Inorganic Chemistry

pubs.acs.org/IC Article

Noncentrosymmetric γ-$Cs_2I_4O_{11}$ Obtained from IO_4 Polyhedral Rearrangements in the Centrosymmetric β-Phase

Ming-Li Liang, Matthew Lacroix, Ce Tao, Michael J. Waters, James M. Rondinelli, and P. Shiv Halasyamani*

Cite This: https://doi.org/10.1021/acs.inorgchem.2c04450 Read Online

ACCESS | Metrics & More | Article Recommendations | Supporting Information

ABSTRACT: We report the synthesis and optical properties of noncentrosymmetric (NCS) γ-$Cs_2I_4O_{11}$ that was obtained through IO_4 polyhedral rearrangements from centrosymmetric (CS) β-$Cs_2I_4O_{11}$. Trifluoroacetic acid (TFA) acts as a structure-directing agent and plays a key role in the synthesis. It is suggested that the function of TFA is to promote rearrangement reactions found in the organic synthesis of stereoisomers. γ-$Cs_2I_4O_{11}$ crystallizes in the NCS monoclinic space group $P2_1$ (No. 4) and exhibits a strong second-harmonic-generation (SHG) response of 5.0 × KDP (KH_2PO_4) under 1064 nm laser radiation. Additional SHG experiments indicate that the material is type I phase matchable. First-principles calculations show that SHG intensity mainly comes from its d_{34}, d_{21}, and d_{23} SHG tensor components. The synthetic strategy of discovering γ-$Cs_2I_4O_{11}$ provides a new way for designing novel NCS SHG materials.

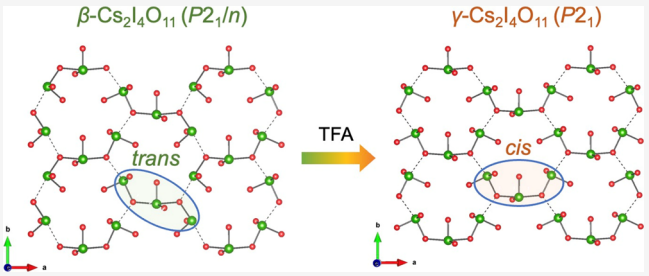

1. INTRODUCTION

Laser technology is used in modern lighting, manufacturing processes, optical fiber communication, and surgery.[1,2] Commercial solid-state lasers, however, are often limited to operating at a single wavelength, limiting their tunability for multiple applications. Second-harmonic-generation (SHG) materials provide one solution to this problem because they can double the frequency of the laser to access shorter wavelengths.[3−6] To date, β-BaB_2O_4 (BBO), KH_2PO_4 (KDP), $KTiOPO_4$ (KTP), $LiNbO_3$ (LN), and $AgGaS_2$ (AGS) are used in solid-state devices ranging from the deep-ultraviolet (deep-UV) through the infrared (IR).[7−13] Nonetheless, compounds with large SHG responses continue to be discovered owing to an increased demand for laser devices at difficult-to-access wavelengths from solid-state sources. Examples of such materials include fluoro-carbonates ($CsPbCO_3F$ − 13.0 × KDP, $RbMgCO_3F$ − 160 × α-SiO_2),[14,15] nitrates ($Pb_2(BO_3)(NO_3)$ − 9.0 × KDP, $Bi_2O_2(NO_3)(OH)$ − 6.0 × KDP),[16,17] and materials containing second-order Jahn−Teller cations ($BaTeMo_2O_9$ − 600 × α-SiO_2, $BaNbO(IO_3)_5$ − 14.0 × KDP, $BiOIO_3$ − 12.5 × KDP, and $BiFSeO_3$ − 13.5 × KDP).[18−21]

For the design of SHG materials, crystallization in a noncentrosymmetric (NCS) space group is necessary. However, fewer than one-fifth of reported inorganic compounds are NCS.[22] Targeted synthesis of NCS compounds has been a goal of many researchers.[23,24] In the past two decades, an often used strategy was to introduce two kinds of local asymmetric units, distorted d^0 transition metal (TM) oxygen octahedra (MoO_6, VO_6, NbO_6, TiO_6, etc.), or lone-pair oxyacids (IO_3, TeO_3, SeO_3, SbO_3, etc.), into the compounds. The idea being that their local asymmetries would result in an NCS structure.[25−28] Based on this strategy, a number of NCS compounds with large SHG responses have been discovered.[10,29−32] Nonetheless, centrosymmetric (CS) materials remain more prevalent compared with NCS materials because these asymmetric units can align in an antiparallel manner.[32] In addition, cation size, hydrogen-bonding interactions, and framework flexibility are also important factors impacting the formation of NCS structures.[32−35]

We describe a new strategy for obtaining an NCS structure. We successfully converted β-$Cs_2I_4O_{11}$ (CS space group $P2_1/n$) directly into a new γ-$Cs_2I_4O_{11}$ (NCS space group $P2_1$), using trifluoroacetic acid (TFA). Upon comparing their structures, we find that the $I_3O_{10}^{5-}$ trimers in the β phase rearrange to a "*cis*-type" arrangement from a "*trans*-type" configuration. We attribute this rearrangement to the structure-directing properties of TFA, which is well known in organic synthesis for intramolecular stereochemistry.[36−38] Further, we compared the physical properties of β- and γ-$Cs_2I_4O_{11}$, including thermogravimetry/differential thermal analysis (TG/DTA), ultraviolet−visible−near infrared (UV−vis−NIR), and infrared

Received: December 20, 2022

https://doi.org/10.1021/acs.inorgchem.2c04450
Inorg. Chem. XXXX, XXX, XXX−XXX

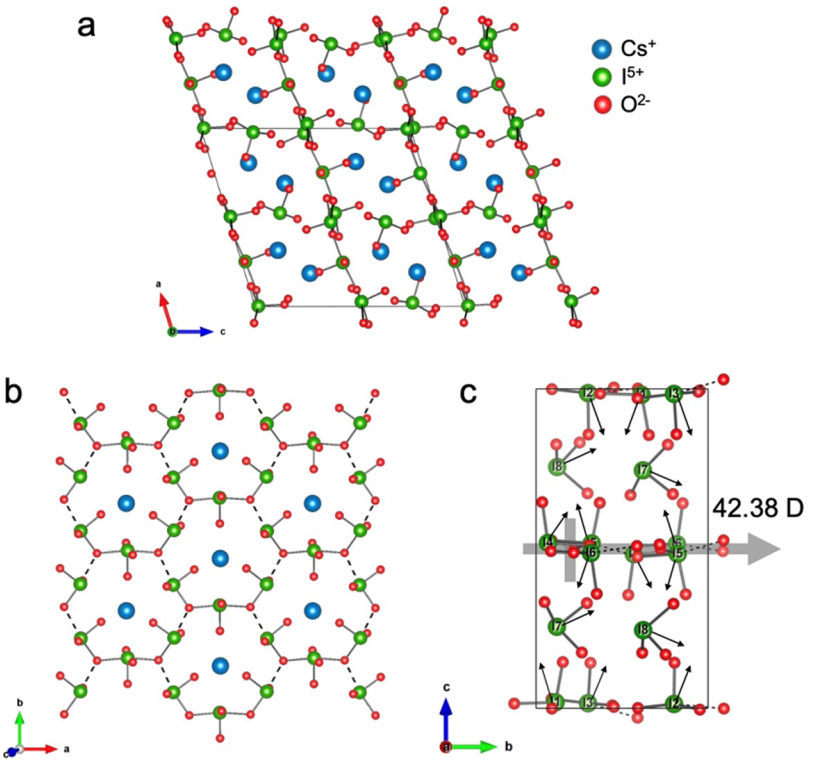

Figure 1. Structure of γ-$Cs_2I_4O_{11}$ in the *ac*-plane (a); 2D HTO-like $[I_3O_8^-]_\infty$ layers consisting of IO_4 six-membered rings (b), dashed lines indicate weak I−O interactions owing to the long bond distances; local and net dipole moment directions of I−O polyhedra in a whole unit cell (c).

(IR) absorptions. SHG measurements of γ-$Cs_2I_4O_{11}$ were also performed. We demonstrate that γ-$Cs_2I_4O_{11}$ is SHG active at 1064 nm with an SHG intensity of 5.0 × KDP. Additional measurements revealed that the material is type I phase matchable.[39] These results indicate that γ-$Cs_2I_4O_{11}$ is a technologically viable SHG material.

2. EXPERIMENTAL SECTION

2.1. Reagents. The chemical reagents Cs_2CO_3 (99%, Alfa Aesar), I_2O_5 (98%, Alfa Aesar), and TFA (99%, Alfa Aesar) were purchased from ThermoFisher Scientific Company and used without further treatment.

2.2. Syntheses of γ-$Cs_2I_4O_{11}$ by Hydrothermal Reactions. *2.2.1. One-Step Method.* Cs_2CO_3 (2.0 mmol, 0.652 g), I_2O_5 (2.5 mmol, 0.835 g), 2.0 mL of deionized water, and 2.0 mL of TFA were loaded into a 23 mL Teflon-lined autoclave. The autoclave was closed and slowly heated to 220 °C. After 4 days at 220 °C, the autoclave was slowly cooled to 25 °C at a rate of 4 °C/h. The solid from the autoclave was washed three times with deionized water to obtain a pure phase of γ-$Cs_2I_4O_{11}$. The average yield is about 85% (based on I_2O_5). Single crystals obtained by this method were used for structural analysis.

2.2.2. Two-Step Method. Cs_2CO_3 (2.0 mmol, 0.652 g), I_2O_5 (2.5 mmol, 0.835 g), and 2.0 mL of deionized water were loaded into a 23 mL Teflon-lined autoclave and closed. With this step, no TFA was used. After 4 days at a constant temperature of 220 °C, the autoclaves were slowly cooled to 25 °C at a rate of 4 °C/h. The solid from the autoclave was washed three times with deionized water to obtain the pure phase of β-$Cs_2I_4O_{11}$. Subsequently, 0.950 g (1.0 mmol) β-$Cs_2I_4O_{11}$ crystals were placed into a 23 mL Teflon-lined autoclave and with 3.0 mL of 80% TFA aqueous solution. The autoclave was closed and heated to 100 °C for 6 h. After this time, all the β-$Cs_2I_4O_{11}$ crystals were completely converted to γ-$Cs_2I_4O_1$ with a final mass of 0.780 g. The yield is about 82% (based on β-$Cs_2I_4O_{11}$).

The purities of β- and γ-$Cs_2I_4O_{11}$ were verified by powder X-ray diffraction (XRD) patterns (Figure S1). Both the initial and final solutions of β- and γ-$Cs_2I_4O_{11}$ synthesis show strong acidic media properties with pH ≈ 0 (Figure S2). This indicates that the addition of TFA does not impact the pH.

2.3. Powder X-ray Diffraction. Powder XRD patterns were recorded on a PANalytical Empyrean diffractometer with graphite-monochromated Cu Kα radiation in the 2θ range of 5−60° at room temperature.

2.4. Thermal Analysis. Thermogravimetric (TG) analyses were performed with an EXSTAR 6300 TG/DTA instrument under a N_2 atmosphere between 30 and 800 °C at a heating rate of 10 °C/min.

2.5. Optical Measurements. IR spectra were recorded on a Thermo Scientific FT-IR spectrometer ranging from 4000 to 400 cm^{-1}. UV−vis−NIR spectra in the range of 200−2500 nm were recorded on an Agilent Technologies Cary Series 5000 UV−vis−NIR spectrophotometer. The UV−vis−NIR absorption spectrum was calculated from the reflectance spectrum using the Kubelka−Munk function: $\alpha/S = (1 - R)^2/2R$, where α is the absorption coefficient, S is the scattering coefficient, and R is the reflectance, respectively.[40]

2.6. Single-Crystal Structure Determination. Single-crystal X-ray diffraction data for γ-$Cs_2I_4O_{11}$ were collected on a Bruker SMART APEX2 diffractometer equipped with a CCD detector (graphite-monochromated Mo Kα radiation, λ = 0.71073 Å) at room temperature. The SAINT program was applied for data reduction and integration. The structure was determined by the direct methods refined by full-matrix least-squares fitting on F^2 using SHELXL-97.[41] All the atoms were refined with anisotropic thermal parameters. The refined *Flack* parameter of 0.00(3) for γ-$Cs_2I_4O_{11}$ is close to zero, indicative of correctness of its absolute structure.[42] The structure was checked for missing symmetry elements using PLATON. Crystallographic data and structural refinements of γ-$Cs_2I_4O_{11}$ are listed in Table S1. The atomic coordinates, selected bond distances, and angles are listed in Tables S2−S4.

2.7. Second-Harmonic-Generation Measurements. Powder SHG measurements were performed on a Q-switched Nd/YAG laser generating radiation at 1064 nm. Crystalline samples of γ-$Cs_2I_4O_{11}$ in the particle-size range of 125−150 μm were used for SHG measurements. To test their phase matching ability, γ-$Cs_2I_4O_{11}$

https://doi.org/10.1021/acs.inorgchem.2c04450
Inorg. Chem. XXXX, XXX, XXX−XXX

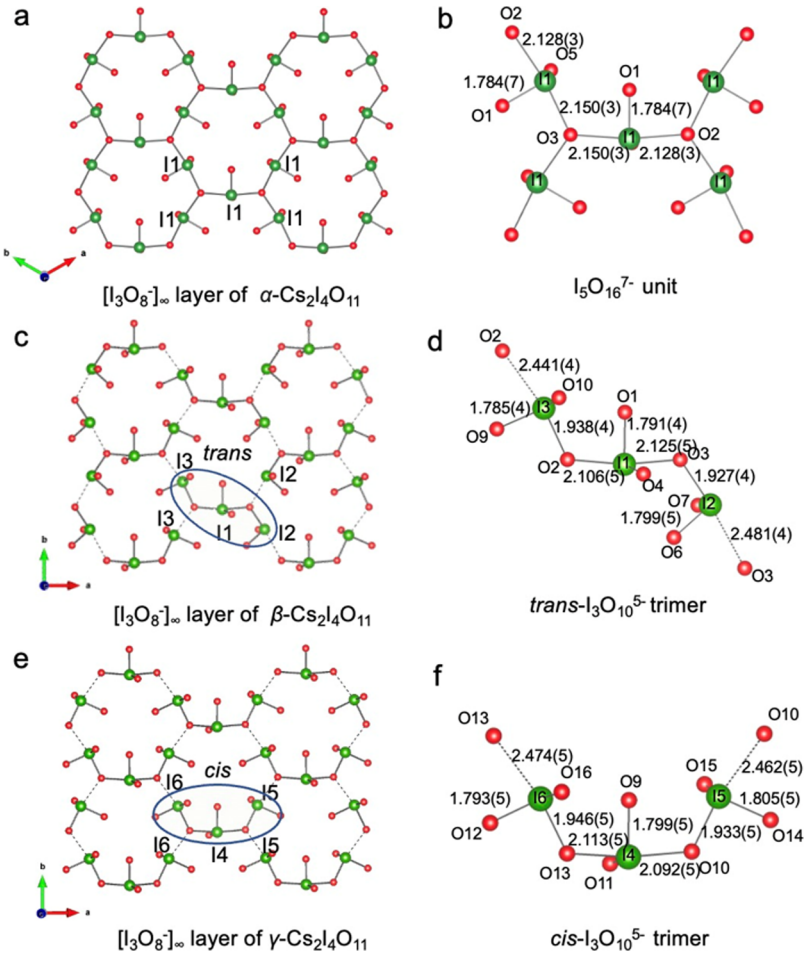

Figure 2. 2D HTO-like $[I_3O_8^-]_\infty$ layers of α-, β-, and γ-$Cs_2I_4O_{11}$ in the *ab*-plane (a, c, e); coordination of the $I_5O_{16}^{7-}$ unit, *trans*- and *cis*-$I_3O_{10}^{5-}$ trimers, respectively (b, d, f). Long I−O distances are indicated with dashed lines.

crystals were sieved into distinct particle-size ranges (<20, 20−45, 45−63, 63−75, 75−95, 95−125, and 125−150 μm). Sieved KDP in the same particle-size ranges were used as references.

2.8. DFT Calculations. First-principles calculations were performed with grid-based projector augmented wave (GPAW) version 22.1.1b1 using density functional theory (DFT) with the Perdew−Burke−Ernzerhof density functional.[43−45] Simulation pre/post-processing was performed with the atomic simulation environment version 3.23.0b1.[46] The pseudopotentials were taken from the standard GPAW pseudopotential set v0.9.20000. Structural optimization and relative formation energy calculations were performed with a 600 eV plane wave cutoff. Optical property calculations were performed with the experimentally resolved γ-phase unit cell and a plane wave cutoff of 500 eV and a scissor shift of 626 meV to compensate for the well-known underprediction of the band gap by DFT. In all electronic structure calculations, the augmentation grid spacing was fixed at 2× the plane wave spacing, Γ-centered *k*-point grids were employed, and the electronic solver convergence criteria between steps were 10^{-7} eV for eigenvalues, 10^{-5} for charge density, and 10^{-4} eV/Å for forces.

Relative formation energy calculations were performed with the optimized, i.e., relaxed, unit cells. Structure optimization was performed including lattice vectors until no force exceeded 5 meV/Å. Structure optimization was repeated with relaxed structures to ensure that dilation of the plane wave basis from cell relaxations did not affect the results. The *k*-point grid used for the α-phase was 8 × 8 × 4 and 4 × 8 × 4 for the β and γ phases owing to the different unit cell sizes, which corresponds to an approximate *k*-point density of ∼150,000 *k*-points per reciprocal Å^3. For linear optical property calculations of the γ-phase, the number of bands included was 3× the number of occupied bands and a *k*-point grid of 2 × 4 × 2 was used since it was found to be well converged. Single particle excitations up to 40 eV were included, and the Coulomb kernel cutoff for local field effects in the random phase approximation was also 40 eV. Linear optical properties are computed from the long wavelength limit of the microscopic dielectric matrix.[47]

SHG calculations of the γ-phase were performed within the length-gauge independent particle approximation using a maximum frequency of 10 eV.[48] The number of bands included was 2× the number of occupied bands. The Brillouin zone (BZ) was sampled with *k*-point grids of 2 × 4 × 2 and 4 × 8 × 4 with ∼4% change in the static ($\omega \rightarrow 0$) second-order polarizabilities so we report the results from the finer grid. Since second-order polarizabilities are an average over the BZ in the independent particle approximation, the band path-decomposed second-order polarizabilities reflect the bulk value if the BZ was represented by each *k*-point along the path.

3. RESULTS AND DISCUSSION

γ-$Cs_2I_4O_{11}$ crystallizes in the NCS space group $P2_1$ (No. 4, Table S1), and its structure is shown in Figure 1a. γ-$Cs_2I_4O_{11}$ exhibits a two-dimensional (2D) hexagonal tungsten oxide (HTO)-like $[I_3O_8^-]_\infty$ layer consisting of IO_4 six-membered rings separated by Cs^+ cations and IO_3^- anions (Figure 1b). There are four Cs, eight I, and twenty-two O atoms in the asymmetric unit. The atomic coordinates and equivalent isotropic displacement parameters are listed in Table S2. Six I atoms, I(1) to I(6), are each coordinated to four oxygen atoms, and form distorted IO_4 tetragonal pyramids. The I−O

https://doi.org/10.1021/acs.inorgchem.2c04450
Inorg. Chem. XXXX, XXX, XXX−XXX

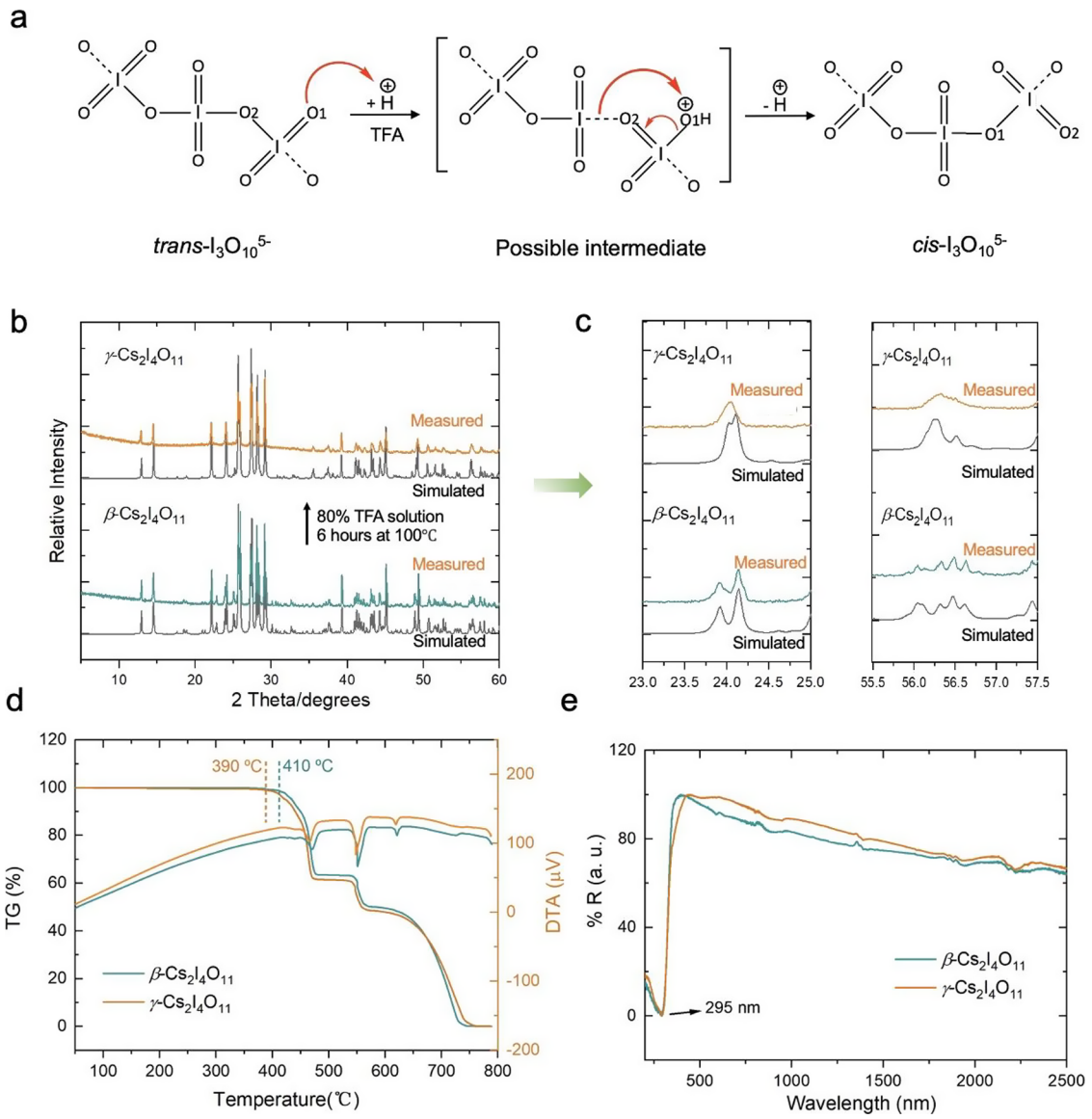

Figure 3. Schematic of the process of IO_4 polyhedral rearrangement with a possible intermediate (a); simulated powder XRD and measured powder XRD of β- and γ-$Cs_2I_4O_{11}$ (b); and their magnified area corresponding to the differences between them (c); the TG and DTA curves of β- and γ-$Cs_2I_4O_{11}$ (d); and the UV−vis−NIR spectra of β- and γ-$Cs_2I_4O_{11}$ (e).

bond distances range from 1.775(5) to 2.474(5) Å (Table S3). The weak I−O interactions with bond distances over 2.4 Å are considered reasonable for polyiodates.[49,50] I(7) and I(8), are both coordinated to three oxygen atoms and form distorted IO_3 trigonal pyramids with the I−O bond distances ranging from 1.787(6) to 1.841(6) Å (Table S4). The O−I−O bond angles range from 78.7(2) to 170.49(19)° (Table S4). The Cs^+ cations are ninefold coordinate, with Cs−O bond distances in the range of 3.155(6)−3.632(7) Å (Table S3). Bond valence sum calculations for γ-$Cs_2I_4O_{11}$ result in values of 0.78−0.84, 4.89−5.04, and −1.70 to −2.23 for Cs, I, and O atoms, respectively, consistent with their oxidation states of +1, +5, and −2 (Table S2).[51,52]

Structurally, distorted IO_3 and IO_4 polyhedra with stereoactive lone pairs tend to have large dipole moments, which are believed to be the main source of the SHG efficiency of iodates.[10,20] Therefore, the local dipole moments as well as the net dipole moments of the unit cell for γ-$Cs_2I_4O_{11}$ were calculated from the geometric structure method reported earlier (Table S5).[53,54] The lone pairs are given a charge of −2 and localized 1.23 Å away from the I^{5+} cations.[55] There are four IO_3 and twelve IO_4 polyhedra in the unit cell. The calculated local dipole moments of IO_3 and IO_4 polyhedra range from 14.33 to 14.47 D and 11.72 to 13.23 D, respectively. Furthermore, the calculated *x*- and *z*-components of the polarizations of all the IO_3 and IO_4 polyhedra sum to zero, i.e., they cancel out and provide no net contribution to the total dipole moment. Only the *y*-components constructively add to a nonzero value of 42.38 D, consistent with the monoclinic symmetry of the γ phase. Among them, $I(2)O_4$, $I(3)O_4$, $I(4)O_4$, $I(7)O_3$, and $I(8)O_3$ polyhedra are aligned toward the +*y* direction (81.1 D), whereas the $I(1)O_4$, $I(5)O_4$, and $I(6)O_4$ polyhedra are aligned oppositely and toward the −*y* direction (−38.72 D). Hence, in the entire unit cell of γ-$Cs_2I_4O_{11}$, there is only a net dipole moment of 42.38 D along the *b* axis (Figure 1c).

The unit cell parameters of α-, β-, and γ-$Cs_2I_4O_{11}$ are listed in Table S1.[49,56] α-$Cs_2I_4O_{11}$ crystallizes in the hexagonal NCS

https://doi.org/10.1021/acs.inorgchem.2c04450
Inorg. Chem. XXXX, XXX, XXX−XXX

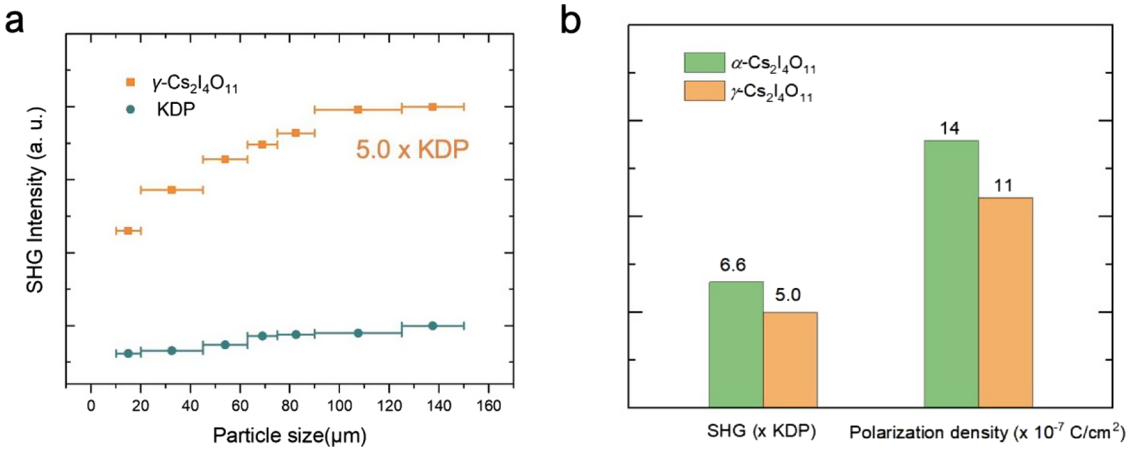

Figure 4. Measured SHG intensities of γ-$Cs_2I_4O_{11}$ and KDP with different particle sizes at 1064 nm (a) and comparisons of SHG intensities and polarization densities of α- and γ-$Cs_2I_4O_{11}$ (b).

space group $P6_3$ (No. 173). β-$Cs_2I_4O_{11}$ crystallizes in the monoclinic CS space group $P2_1/n$ (No. 14). β- and γ-$Cs_2I_4O_{11}$ have almost identical unit cell parameters and very similar structures. For their symmetry elements, an inversion center $(-x, -y, -z)$, 2_1 screw axis $(1/2 - x, 1/2 + y, 1/2 - z)$, and an n-glide plane $(1/2 + x, 1/2 - y, 1/2 + z)$ exist simultaneously in the β-phase structure (Figure S3a), whereas only the 2_1 screw axis $(-x, 1/2 + y, -z)$ persists in the NCS γ-phase (Figure S3b). The glide plane in the β-$Cs_2I_4O_{11}$ structure is perpendicular to the b axis and located at (1/2 0 1/2) as shown in Figure S2c. At the same location, a glide plane cannot occur in the γ-$Cs_2I_4O_{11}$ structure (Figure S3d).

There are 2D HTO-like $[I_3O_8^-]_\infty$ layers in all α-, β-, and γ-$Cs_2I_4O_{11}$ structures (Figure 2). In the α-$Cs_2I_4O_{11}$ structure, there is only one type of I atom, I(1), with I−O bond distances ranging from 1.784(7) to 2.150(3) Å (Figure 2a,b). However, there are three different types of I atoms in the $[I_3O_8^-]_\infty$ layer of β- and γ-$Cs_2I_4O_{11}$. In the β-$Cs_2I_4O_{11}$, the $I(1)O_4$, $I(2)O_4$, and $I(3)O_4$ polyhedra are corner-shared to form a *trans*-$I_3O_{10}^{5-}$ trimer (Figure 2c,d), whereas in the γ-$Cs_2I_4O_{11}$ structure, the $I(4)O_4$, $I(5)O_4$, and $I(6)O_4$ polyhedra are corner-shared to form a *cis*-$I_3O_{10}^{5-}$ trimer (Figure 2e,f). Here, the backbone bonds correspond to strong I−O interactions with bond distances between 1.927(4) and 2.125(5) Å.

The differences in the structures of α-, β-, and γ-$Cs_2I_4O_{11}$ stem from their different synthetic methods. For α-$Cs_2I_4O_{11}$ synthesis, Nb_2O_5 plays an important role but with an unclear mechanism.[49] By comparing the β- and γ-$Cs_2I_4O_{11}$ synthesis, we found that TFA plays a key role in the isomeric control of the trimeric units (see Section 2). Under identical conditions, the addition of TFA resulted in the formation of γ-$Cs_2I_4O_{11}$, and the absence of TFA resulted in the formation of β-$Cs_2I_4O_{11}$. Interestingly, we found that β-$Cs_2I_4O_{11}$ can be directly converted to γ-$Cs_2I_4O_{11}$ by TFA at a lower temperature (100 °C). In other words, the *trans*-$I_3O_{10}^{5-}$ trimers were converted to *cis*-$I_3O_{10}^{5-}$ trimers through the structure-directing properties of TFA, which is widely used as a functional group rearrangement reagent in organic synthesis owing to its large acid ionization constant (K_a).[36−38,57] It can easily promote the protonation of O atoms in functional groups, further triggering rearrangement reactions.[36,37] Herein, we suggest a mechanism to describe the possible IO_4 polyhedral rearrangement (Figure 3a). With it, O2 is replaced by O1 under the action of a proton and causes a reversal of the orientation of the IO_4 polyhedron. Thus, the *trans*-$I_3O_{10}^{5-}$ trimer converts to the *cis*-$I_3O_{10}^{5-}$ trimer. In addition, we have attempted to convert α-$Cs_2I_4O_{11}$ to γ-$Cs_2I_4O_{11}$ using the two-step method but were unsuccessful. The powder XRD measurements before and after the reaction were essentially indistinguishable (Figure S4). A possible reason is that I−O bonds in its 2D HTO-like skeletons are all strong interactions (Figure 2b), which hinders the inversion of the I−O polyhedra.

The powder XRD patterns of β- and γ-$Cs_2I_4O_{11}$ are shown in Figure 3b, where the γ-$Cs_2I_4O_{11}$ crystals were converted from the β-$Cs_2I_4O_{11}$ crystals using the "two-step method". By comparing their characteristic peaks in the diffraction patterns in the 23−25° and 55.5−57.5° 2θ regions (Figure 3c), we found that the measured powder XRD of the converted γ-$Cs_2I_4O_{11}$ and the simulated XRD are in good agreement. TG/DTA measurements showed that the decomposition processes for β- and γ-$Cs_2I_4O_{11}$ are slightly different (Figure 3d). There are three mass loss steps between 30 and 800 °C for both phases. The mass of γ-$Cs_2I_4O_{11}$ was unchanged before 390 °C, and the mass of β-$Cs_2I_4O_{11}$ was unchanged before 410 °C. The first step likely corresponds to the release of two IO_3^- anions (cal: 36.8%, exp: 36.7%) for β-$Cs_2I_4O_{11}$, one IO_3^- anion and one IO_4^{3-} anion (cal: 38.5%, exp: 38.4%) for γ-$Cs_2I_4O_{11}$. The second step corresponds to the release of one Cs^+ (cal: 14.0%, exp: 14.1%). The remaining constituents are completely released in their third step. In addition, we did not observe any peaks before 410 °C in either DTA trace. This suggests that the conversion from β- to γ-$Cs_2I_4O_{11}$ is not attributable to a first-order phase transition.

UV−vis−NIR reflectance spectra showed strong absorption in the UV region with a maximum at 295 nm for both β- and γ-$Cs_2I_4O_{11}$ (Figure 3e), and broad transparent ranges at 395−2500 and 420−2500 nm, respectively. The optical band gap (E_g) was determined to be about 3.74 eV for both phases (Figure S5), making them wide-band-gap semiconductors. FT-IR spectra of β- and γ-$Cs_2I_4O_{11}$ were not significantly different, with all the peak positions corresponding well. The assignment of these peaks is shown in Figure S6. The FT-IR spectra show no absorption between 4.0 and 11.1 μm (2500 and 900 cm^{-1}) for both β- and γ-$Cs_2I_4O_{11}$, consistent with reported anhydrous iodates.[58−60]

Powder SHG measurements showed that γ-$Cs_2I_4O_{11}$ can exhibit a strong 532 nm signal when irradiated by a 1064 nm

https://doi.org/10.1021/acs.inorgchem.2c04450
Inorg. Chem. XXXX, XXX, XXX−XXX

laser. The SHG signal is about 5.0 × KDP (Figures 4a and S6). SHG intensity vs particle size experiments revealed that γ-$Cs_2I_4O_{11}$ exhibits type-I phase matching under 1064 nm irradiation (Figure 4a).[39] The SHG intensity is much higher than other reported polyiodates, such as $Bi_4O(I_3O_{10})$-$(IO_3)_3(SeO_4)$ (1.1 × KDP),[61] $HBa_{2.5}(IO_3)_6(I_2O_5)$ (1.6 × KDP),[62] $Ba_4Ag_5(IO_3)_6(I_3O_8)_3(I_4O_{11})_2$ (2.5 × KDP),[63] and comparable to those of α-$Cs_2I_4O_{11}$ (300 × α-SiO_2),[49] and $K_2Na(IO_3)_2(I_3O_8)$ (7.6 × KDP).[64] However, it is not as large as YI_5O_{14} (14.0 × KDP),[65] GdI_5O_{14} (15.0 × KDP),[65] or NaI_3O_8 (18.7 × KDP).[66] The differences in SHG intensities are from the macroscopic polarizations of their respective structures.[20] A detailed comparison of γ-$Cs_2I_4O_{11}$ and α-$Cs_2I_4O_{11}$ was further made to better understand the structure-related SHG properties. For comparison purposes, we re-measured the SHG signal with KDP as a reference. The result shows that the SHG intensity of α-$Cs_2I_4O_{11}$ is 6.6 × KDP (Figure S7), that is slightly larger than that of γ-$Cs_2I_4O_{11}$ (Figure 4b). We compared their net dipole moments in their entire unit cells (Table S5). Unlike γ-$Cs_2I_4O_{11}$ with a net dipole moment of 42.38 D along the *b* axis, there is a net dipole moment of 27.16 D along the *c* axis for α-$Cs_2I_4O_{11}$ (Figure S8). Further, we calculated the macroscopic polarization using nominal valences and by dividing the net dipole moments by their unit cell volumes.[67,68] The calculated values of them are approximately 1.4×10^{-6} and 1.1×10^{-6} C/cm^2 for α- and γ-$Cs_2I_4O_{11}$, respectively (Figure 4b). The trend positive correlation between the SHG intensities and polarization densities indicates that the larger SHG response of α-$Cs_2I_4O_{11}$ originates from its larger polarization density.

DFT calculations of the relative formation enthalpies at 0 K of the α-, β-, and γ-$Cs_2I_4O_{11}$ were performed using the relaxed structures. We find that the β phase is the lowest enthalpy structure and that the α and γ phases are 4.6 and 0.9 meV/atom higher in energy. Considering such small relative formation enthalpies, vibrational entropy contributions to the free energy are likely needed to determine the relative phase stability at room temperature. Likewise, with such a small formation energy difference between β- and γ-$Cs_2I_4O_{11}$, a higher level of theory may be required to confirm the relative stability. Regardless, the DFT calculations indicate that the α, β, and γ phases have only small formation energy differences and are consistent with experimental conversion between polymorphs.

Using the experimentally determined γ-$Cs_2I_4O_{11}$ structure, the electronic structure band structure, projected density of states, and optical properties were calculated. The valence band maximum is at the Γ-point, and the conduction band minimum is at the *E*-point, giving an indirect band gap of 3.114 eV (Figure 5a) that is smaller than the experimental (3.74 eV) owing to the limitations of the DFT methods.[69] The orbital-projected density of states shows the valence bands comprise oxygen *p*-states with a small hybridization with iodine *s*- and *p*-states (Figure 5b). The majority of iodine states are associated with the conduction bands. The cesium *s* states are above the plotted range and empty. Overall, the PDOS follows chemical intuition, showing fully ionized cesium atoms, and sp^3 hybridization of the iodine atoms bonded to oxygen with some degree of bond ionicity.

While the full frequency-dependent linear optical and second-order polarizability properties calculated are presented in Figures S9−S11. The calculated birefringence (Δ*n*) of γ-$Cs_2I_4O_{11}$ is 0.055 at 1064 nm (Figure S10), which is similar to

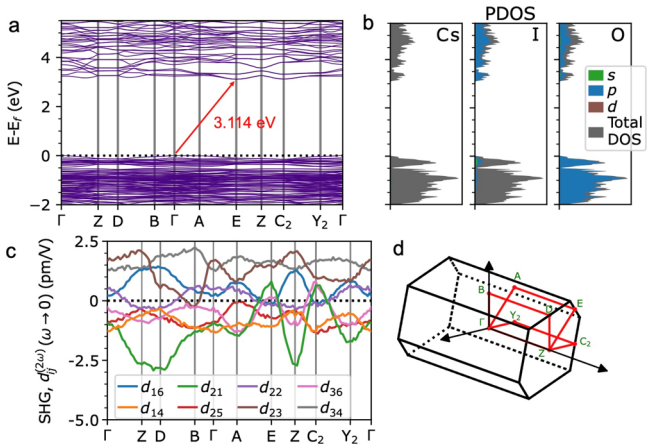

Figure 5. Calculated electronic band structure of γ-$Cs_2I_4O_{11}$ (a); the total and partial orbital-projected density of states for γ-$Cs_2I_4O_{11}$ (b); and the distribution of contributions to d_{ij} along the band path (c) and the band path plotted in the Brillouin zone (d).

other reported polyiodates.[63−65] The long wavelength limit (ω → 0) of the second-order polarizability tensor elements are presented in Figure 5c and Table 1. Since the calculations include dispersion, there are eight independent tensor elements for the $P2_1$ space group rather than the four that would be expected with the Kleinman symmetry. The results show that d_{34}, d_{21}, and d_{23} SHG tensors exhibit large contributions with values of 1.69, −1.20, and 1.07 pm/V, respectively. They are considered to be the main source of the SHG response of γ-$Cs_2I_4O_{11}$. When comparing the largest tensor elements to their BZ decomposition in Figure 5d, a key feature is the lack of sign changes with respect to the moment vector highlighting the importance of the geometric phase in obtaining a large SHG response.

Table 1. Long Wavelength Limit (ω → 0) SHG Tensor Components, d_{ij}, of γ-$Cs_2I_4O_{11}$ Calculated from First Principles without Kleinman Symmetry

SHG tensor components	values (pm/V)	SHG tensor components	values (pm/V)
d_{14}	−0.89	d_{23}	1.07
d_{16}	0.55	d_{25}	−0.79
d_{21}	−1.20	d_{34}	1.69
d_{22}	0.11	d_{36}	−0.50

4. CONCLUSIONS

In this work, a new NCS cesium iodate, namely, γ-$Cs_2I_4O_{11}$, has been synthesized successfully. It can be converted from the CS β-$Cs_2I_4O_{11}$ by IO_4 polyhedral rearrangements under the structure-directing action of TFA. Concretely, a *trans*-$I_3O_{10}^{5-}$ trimer turns into a *cis*-$I_3O_{10}^{5-}$ trimer in their structures. In addition, γ-$Cs_2I_4O_{11}$ has exhibited high thermal stability, a broad transparent range, and a very strong SHG response. The experimental results showed that its SHG response is 5.0 times that of KDP, with type I phase matching. Our work provides a way for iodate conversion from CS to NCS phases and demonstrates the potential of γ-$Cs_2I_4O_{11}$ as a good SHG material.

https://doi.org/10.1021/acs.inorgchem.2c04450
Inorg. Chem. XXXX, XXX, XXX−XXX

■ ASSOCIATED CONTENT

Supporting Information

The Supporting Information is available free of charge at https://pubs.acs.org/doi/10.1021/acs.inorgchem.2c04450.

Crystal data (cif-file), atomic coordinates, important bond distances and angles, calculated local dipole moments, powder XRD, pH measurements, optical band gaps, IR spectra, the full frequency-dependent linear optical, and second-order polarizability properties of the γ-$Cs_2I_4O_{11}$ (PDF)

Accession Codes

CCDC 2226590 contains the supplementary crystallographic data for this paper. These data can be obtained free of charge via www.ccdc.cam.ac.uk/data_request/cif, or by emailing data_request@ccdc.cam.ac.uk, or by contacting The Cambridge Crystallographic Data Centre, 12 Union Road, Cambridge CB2 1EZ, UK; fax: +44 1223 336033.

CCDC 2226590 contains the supplementary crystallographic data for this work. These data can be obtained free of charge via https://www.ccdc.cam.ac.uk/structures/?, or by emailing data_request@ccdc.cam.ac.uk, or by contacting The Cambridge Crystallographic Data Centre, 12 Union Road, Cambridge CB2 1EZ, UK; fax: +44 1223 336033.

■ AUTHOR INFORMATION

Corresponding Author

P. Shiv Halasyamani − *Department of Chemistry, University of Houston, Houston, Texas 77204, United States;* orcid.org/0000-0003-1787-1040; Email: pshiv@central.uh.edu

Authors

Ming-Li Liang − *Department of Chemistry, University of Houston, Houston, Texas 77204, United States*

Matthew Lacroix − *Department of Chemistry, University of Houston, Houston, Texas 77204, United States*

Ce Tao − *Department of Chemistry, University of Houston, Houston, Texas 77204, United States*

Michael J. Waters − *Department of Materials Science and Engineering, Northwestern University, Evanston, Illinois 60208, United States;* orcid.org/0000-0001-6425-4331

James M. Rondinelli − *Department of Materials Science and Engineering, Northwestern University, Evanston, Illinois 60208, United States;* orcid.org/0000-0003-0508-2175

Complete contact information is available at: https://pubs.acs.org/10.1021/acs.inorgchem.2c04450

Notes

The authors declare no competing financial interest.

■ ACKNOWLEDGMENTS

M.-L.L., M.L., C.T., and P.S.H. thank the Welch Foundation (Grant E-1457) and the NSF (DMR − 2002319) for their support. The computational work by M.J.W. and J.M.R. was supported by the National Science Foundation (NSF) Grant no. DMR-2011208 and used resources of the National Energy Research Scientific Computing Center (NERSC), a U.S. DOE Office of Science User Facility located at Lawrence Berkeley National Laboratory, operated under Contract no. DE-AC02-05CH11231.

■ REFERENCES

(1) Slusher, R. E. Laser Technology. *Rev. Mod. Phys.* **1999**, *71*, 471−478.

(2) Walsh, L. J. The Current Status of Laser Applications in Dentistry. *Aust. Dent. J.* **2003**, *48*, 146−155.

(3) Mutailipu, M.; Poeppelmeier, K. R.; Pan, S. Borates: A Rich Source for Optical Materials. *Chem. Rev.* **2021**, *121*, 1130−1202.

(4) Fiore, A.; Berger, V.; Rosencher, E.; Bravetti, P.; Nagle, J. Phasematchingusing an Isotropicnonlinear Opticalmaterial. *Nature* **1998**, *391*, 463−466.

(5) Shi, G.; Wang, Y.; Zhang, F.; Zhang, B.; Yang, Z.; Hou, X.; Pan, S.; Poeppelmeier, K. R. Finding the Next Deep-Ultraviolet Nonlinear Optical Material: $NH_4B_4O_6F$. *J. Am. Chem. Soc.* **2017**, *139*, 10645−10648.

(6) Bordui, P. F.; Fejer, M. M. Inorganic Crystals for Nonlinear Optical Frequency Conversion. *Annu. Rev. Mater. Sci.* **1993**, *23*, 321−379.

(7) Chen, C.; Wang, Y.; Wu, B.; Wu, K.; Zeng, W.; Yu, L. Design and synthesis of an ultraviolet-transparent nonlinear optical crystal $Sr_2Be_2B_2O_7$. *Nature* **1995**, *373*, 322−324.

(8) Tran, T. T.; Yu, H.; Rondinelli, J. M.; Poeppelmeier, K. R.; Halasyamani, P. S. Deep Ultraviolet Nonlinear Optical Materials. *Chem. Mater.* **2016**, *28*, 5238−5258.

(9) Mutailipu, M.; Zhang, M.; Yang, Z.; Pan, S. Targeting the Next Generation of Deep-Ultraviolet Nonlinear Optical Materials: Expanding from Borates to Borate Fluorides to Fluorooxoborates. *Acc. Chem. Res.* **2019**, *52*, 791−801.

(10) Chen, J.; Hu, C. L.; Kong, F.; Mao, J. G. High-Performance Second-Harmonic-Generation (SHG) Materials: New Developments and New Strategies. *Acc. Chem. Res.* **2021**, *54*, 2775−2783.

(11) Guo, S. P.; Cheng, X.; Sun, Z. D.; Chi, Y.; Liu, B. W.; Jiang, X. M.; Li, S. F.; Xue, H. G.; Deng, S.; Duppel, V.; Kohler, J.; Guo, G. C. Large Second Harmonic Generation (SHG) Effect and High Laser-Induced Damage Threshold (LIDT) Observed Coexisting in Gallium Selenide. *Angew. Chem., Int. Ed.* **2019**, *58*, 8087−8091.

(12) Okorogu, A. O.; Mirov, S. B.; Lee, W.; Crouthamel, D. I.; Jenkins, N.; Dergachev, Y. A.; Vodopyanov, K. L.; Jenkins, N.; Badikov, V. V. Tunable Middle Infrared Downconversion in GaSe and $AgGaS_2$. *Opt. Commun.* **1998**, *155*, 307−312.

(13) Kang, L.; Liang, F.; Jiang, X.; Lin, Z.; Chen, C. First-Principles Design and Simulations Promote the Development of Nonlinear Optical Crystals. *Acc. Chem. Res.* **2020**, *53*, 209−217.

(14) Zou, G.; Huang, L.; Ye, N.; Lin, C.; Cheng, W.; Huang, H. $CsPbCO_3F$: A Strong Second-Harmonic Generation Material Derived from Enhancement via p-π Interaction. *J. Am. Chem. Soc.* **2013**, *135*, 18560−18566.

(15) Tran, T. T.; He, J.; Rondinelli, J. M.; Halasyamani, P. S. $RbMgCO_3F$: A New Beryllium-Free Deep-Ultraviolet Nonlinear Optical Material. *J. Am. Chem. Soc.* **2015**, *137*, 10504−10507.

(16) Song, J. L.; Hu, C. L.; Xu, X.; Kong, F.; Mao, J. G. A Facile Synthetic Route to A New SHG Material with Two Types of Parallel π-Conjugated Planar Triangular Units. *Angew. Chem., Int. Ed.* **2015**, *54*, 3679−3682.

(17) Huang, H.; He, Y.; Li, X.; Li, M.; Zeng, C.; Dong, F.; Du, X.; Zhang, T.; Zhang, Y. $Bi_2O_2(OH)(NO_3)$ as A Desirable $[Bi_2O_2]^{2+}$ Layered Photocatalyst: Strong Intrinsic Polarity, Rational Band Structure and {001} Active Facets Co-beneficial for Robust Photooxidation Capability. *J. Mater. Chem. A* **2015**, *3*, 24547−24556.

(18) Ra, H. S.; Ok, K. M.; Halasyamani, P. S. Combining Second-Order Jahn-Teller Distorted Cations to Create Highly Efficient SHG Materials: Synthesis, Characterization, and NLO Properties of $BaTeM_2O_9$ (M = Mo^{6+} or W^{6+}). *J. Am. Chem. Soc.* **2003**, *125*, 7764−7765.

(19) Sun, C. F.; Hu, C. L.; Xu, X.; Ling, J. B.; Hu, T.; Kong, F.; Long, X. F.; Mao, J. G. $BaNbO(IO_3)_5$: A New Polar Material with a Very Large SHG Response. *J. Am. Chem. Soc.* **2009**, *131*, 9486−9487.

(20) Nguyen, S. D.; Yeon, J.; Kim, S. H.; Halasyamani, P. S. $BiO(IO_3)$: A New Polar Iodate that Exhibits an Aurivillius-type

$(Bi_2O_2)^{2+}$ Layer and A Large SHG Response. *J. Am. Chem. Soc.* **2011**, *133*, 12422−12425.
(21) Liang, M. L.; Hu, C. L.; Kong, F.; Mao, J. G. $BiFSeO_3$: An Excellent SHG Material Designed by Aliovalent Substitution. *J. Am. Chem. Soc.* **2016**, *138*, 9433−9436.
(22) Simon, F.; Clevers, S.; Dupray, V.; Coquerel, G. Relevance of the Second Harmonic Generation to Characterize Crystalline Samples. *Chem. Eng. Technol.* **2015**, *38*, 971−983.
(23) Halasyamani, P. S.; Poeppelmeier, K. R. Noncentrosymmetric Oxides. *Chem. Mater.* **1998**, *10*, 2753−2769.
(24) Maggard, P. A.; Stern, C. L.; Poeppelmeier, K. R. Understanding the Role of Helical Chains in the Formation of Noncentrosymmetric Solids. *J. Am. Chem. Soc.* **2001**, *123*, 7742−7743.
(25) Ok, K. M.; Chi, E. O.; Halasyamani, P. S. Bulk Characterization Methods for Non-Centrosymmetric Materials: Second-Harmonic Generation, Piezoelectricity, Pyroelectricity, and Ferroelectricity. *Chem. Soc. Rev.* **2006**, *35*, 710−717.
(26) Halasyamani, P. S. Asymmetric Cation Coordination in Oxide Materials: Influence of Lone-Pair Cations on the Intra-octahedral Distortion in d^0 Transition Metals. *Chem. Mater.* **2004**, *16*, 3586−3592.
(27) Liang, M. L.; Ma, Y. X.; Hu, C. L.; Kong, F.; Mao, J. G. $Ba(MoO_2F)_2(QO_3)_2$ (Q = Se, Te): Partial Fluorination of MoO_6 Octahedra Enabling Two Polar Solids with Strong and Phase Matchable SHG Response. *Chem. Mater.* **2020**, *32*, 9688−9695.
(28) Zhou, Y.; Hu, C. L.; Hu, T.; Kong, F.; Mao, J. G. Explorations of New Second-Order NLO Materials in the Ag(I)-Mo(VI)/W(VI)-Te(IV)-O Systems. *Dalton Trans.* **2009**, *29*, 5747−5754.
(29) Zhao, S.; Jiang, X.; He, R.; Zhang, S.; Sun, Z.; Luo, J.; Lin, Z.; Hong, M. A. Combination of Multiple Chromophores Enhances Second-Harmonic Generation in a Nonpolar Noncentrosymmetric Oxide: $CdTeMoO_6$. *J. Mater. Chem. C* **2013**, *1*, 2906−2912.
(30) Li, Y.; Han, G.; Yu, H.; Li, H.; Yang, Z.; Pan, S. Two Polar Molybdenum(VI) Iodates(V) with Large Second-Harmonic Generation Responses. *Chem. Mater.* **2019**, *31*, 2992−3000.
(31) Wu, C.; Lin, L.; Jiang, X.; Lin, Z.; Huang, Z.; Humphrey, M. G.; Halasyamani, P. S.; Zhang, C. $K_5(W_3O_9F_4)(IO_3)$: An Efficient Mid-Infrared Nonlinear Optical Compound with High Laser Damage Threshold. *Chem. Mater.* **2019**, *31*, 10100−10108.
(32) Ok, K. M. Toward the Rational Design of Novel Noncentrosymmetric Materials: Factors Influencing the Framework Structures. *Acc. Chem. Res.* **2016**, *49*, 2774−2785.
(33) Oh, S. J.; Lee, D. W.; Ok, K. M. Influence of the Cation Size on the Framework Structures and Space Group Centricities in $AMo_2O_5(SeO_3)_2$ (A = Sr, Pb, and Ba). *Inorg. Chem.* **2012**, *51*, 5393−5399.
(34) Lee, D. W.; Ok, K. M. New Alkali-Metal Gallium Selenites, $AGa(SeO_3)_2$ (A = Li, Na, K, and Cs): Effect of Cation Size on the Framework Structures and Macroscopic Centricities. *Inorg. Chem.* **2013**, *52*, 5176−5184.
(35) Kim, E.; Lee, D. W.; Ok, K. M. Centrosymmetric $[N(CH_3)_4]_2TiF_6$ vs. Noncentrosymmetric Polar $[C(NH_2)_3]_2TiF_6$: A Hydrogen-Bonding Effect on the Out-of-center Distortion of TiF_6 Octahedra. *J. Solid State Chem.* **2012**, *195*, 149−154.
(36) López, S. E.; Salazar, J. Trifluoroacetic Acid: Uses and Recent Applications in Organic Synthesis. *J. Fluor. Chem.* **2013**, *156*, 73−100.
(37) Dauben, W. G.; Chollet, A. Acid Catalyzed Cope Rearrangements of P-Acyl-1,5-Dienes. *Tetrahedron Lett.* **1981**, *22*, 1583−1586.
(38) Castro, A. M. M. Claisen Rearrangement over the Past Nine Decades. *Chem. Rev.* **2004**, *104*, 2939−3002.
(39) Zhang, W.; Yu, H.; Wu, H.; Halasyamani, P. S. Phase-Matching in Nonlinear Optical Compounds: A Materials Perspective. *Chem. Mater.* **2017**, *29*, 2655−2668.
(40) Sheldrick, G. M. A Short History of SHELX. *Acta Crystallogr. A* **2008**, *64*, 112−122.
(41) Wendland, W. M.; Hecht, H. G. *Reflectance Spectroscopy: Interscience*; J Wiley and Sons, Inc.: New York, 1966.
(42) Flack, H. D.; Bernardinelli, G. The Use of X-ray Crystallography to Determine Absolute Configuration. *Chirality* **2008**, *20*, 681−690.
(43) Enkovaara, J.; Rostgaard, C.; Mortensen, J. J.; Chen, J.; Dulak, M.; Ferrighi, L.; Gavnholt, J.; Glinsvad, C.; Haikola, V.; Hansen, H. A.; Kristoffersen, H. H.; Kuisma, M.; Larsen, A. H.; Lehtovaara, L.; Ljungberg, M.; Lopez-Acevedo, O.; Moses, P. G.; Ojanen, J.; Olsen, T.; Petzold, V.; Romero, N. A.; Stausholm-Moller, J.; Strange, M.; Tritsaris, G. A.; Vanin, M.; Walter, M.; Hammer, B.; Hakkinen, H.; Madsen, G. K.; Nieminen, R. M.; Norskov, J. K.; Puska, M.; Rantala, T. T.; Schiotz, J.; Thygesen, K. S.; Jacobsen, K. W. Electronic Structure Calculations with GPAW: A Real-space Implementation of The Projector Augmented-wave method. *J. Phys. Condens. Matter* **2010**, *22*, No. 253202.
(44) Mortensen, J. J.; Hansen, L. B.; Jacobsen, K. W. Real-space Grid Implementation of The Projector Augmented Wave Method. *Phys. Rev. B* **2005**, *71*, No. 035109.
(45) Perdew, J. P.; Burke, K.; Ernzerhof, M. Generalized Gradient Approximation Made Simple. *Phys. Rev. Lett.* **1996**, *77*, 3865−3868.
(46) Larsen, A. H.; Mortensen, J. J.; Blomqvist, J.; Castelli, I. E.; Christensen, R.; Dułak, M.; Friis, J.; Groves, M. N.; Hammer, B.; Hargus, C.; Hermes, E. D.; Jennings, P. C.; Jensen, P. B.; Kermode, J.; Kitchin, J. R.; Kolsbjerg, E. L.; Kubal, J.; Kaasbjerg, K.; Lysgaard, S.; Maronsson, J. B.; Maxson, T.; Olsen, T.; Pastewka, L.; Peterson, A.; Rostgaard, C.; Schiøtz, J.; Schütt, O.; Strange, M.; Thygesen, K. S.; Vegge, T.; Vilhelmsen, L.; Walter, M.; Zeng, Z.; Jacobsen, K. W. The Atomic Simulation Environment-A Python Library for Working with Atoms. *J. Phys. Condens. Matter* **2017**, *29*, 273002.
(47) Yan, J.; Mortensen, J. J.; Jacobsen, K. W.; Thygesen, K. S. Linear Density Response Function in the Projector Augmented Wave Method: Applications to Solids, Surfaces, and Interfaces. *Phys. Rev. B* **2011**, *83*, No. 245122.
(48) Taghizadeh, A.; Thygesen, K. S.; Pedersen, T. G. Two-Dimensional Materials with Giant Optical Nonlinearities near the Theoretical Upper Limit. *ACS Nano* **2021**, *15*, 7155−7167.
(49) Ok, K. M.; Halasyamani, P. S. The Lone-Pair Cation I^{5+} in a Hexagonal Tungsten Oxide-Like Framework: Synthesis, Structure, and Second-Harmonic Generating Properties of $Cs_2I_4O_{11}$. *Angew. Chem., Int. Ed.* **2004**, *116*, 5605−5607.
(50) Chen, Q. Q.; Hu, C. L.; Chen, J.; Li, Y. L.; Li, B. X.; Mao, J. G. $[o\text{-}C_5H_4NHOH]_2[I_7O_{18}(OH)]_3H_2O$: An Organic-Inorganic Hybrid SHG Material Featuring an $[I_7O_{18}(OH)]$ infinity 2-Branched Polyiodate Chain. *Angew. Chem., Int. Ed.* **2021**, *60*, 17426−17429.
(51) Brese, N.; O'Keeffe, M. Bond-Valence Parameters for Solids. *Acta Crystallogr., Sect. B: Struct. Sci.* **1991**, *47*, 192−197.
(52) Brown, I. D.; Altermatt, D. Bond-valence Parameters Obtained from a Systematic Analysis of the Inorganic Crystal Structure Database. *Acta Crystallogr. Sect. B.* **1985**, *41*, 244−247.
(53) Lee, D. W.; Oh, S. J.; Halasyamani, P. S.; Ok, K. M. New Quaternary Tellurite and Selenite: Synthesis, Structure, and Characterization of Centrosymmetric $InVTe_2O_8$ and Noncentrosymmetric $InVSe_2O_8$. *Inorg. Chem.* **2011**, *50*, 4473−4480.
(54) Xu, X.; Hu, C. L.; Li, B. X.; Yang, B. P.; Mao, J. G. α-AgI_3O_8 and β-AgI_3O_8 with Large SHG Responses: Polymerization of IO_3 Groups into the I_3O_8 Polyiodate Anion. *Chem. Mater.* **2014**, *26*, 3219−3230.
(55) Galy, J.; Meunier, G.; Andersson, S.; Åström, A. Stéréochimie des Eléments Comportant des Paires Non Liées: Ge (II), As (III), Se (IV), Br (V), Sn (II), Sb (III), Te (IV), I (V), Xe (VI), Tl (I), Pb (II), et Bi (III) (Oxydes, Fluorures et Oxyfluorures). *J. Solid State Chem.* **1975**, *13*, 142−159.
(56) Ok, K. M.; Halasyamani, P. S. New Metal Iodates: Syntheses, Structures, and Characterizations of Noncentrosymmetric $La(IO_3)_3$ and $NaYI_4O_{12}$ and Centrosymmetric β-$Cs_2I_4O_{11}$ and $Rb_2I_6O_{15}(OH)_2H_2O$. *Inorg. Chem.* **2005**, *44*, 9353−9359.
(57) Lutz, R. P. Catalysis of the Cope and Claisen Rearrangements. *Chem. Rev.* **1984**, *84*, 205−247.
(58) Mao, F. F.; Hu, C. L.; Xu, X.; Yan, D.; Yang, B. P.; Mao, J. G. $Bi(IO_3)F_2$: The First Metal Iodate Fluoride with a Very Strong

https://doi.org/10.1021/acs.inorgchem.2c04450
Inorg. Chem. XXXX, XXX, XXX−XXX

Second Harmonic Generation Effect. *Agnew. Chem. Int. Ed.* **2017**, *56*, 2151−2155.
(59) Yu, H.; Nisbet, M. L.; Poeppelmeier, K. R. Assisting the Effective Design of Polar Iodates with Early Transition-Metal Oxide Fluoride Anions. *J. Am. Chem. Soc.* **2018**, *140*, 8868−8876.
(60) Chen, J.; Hu, C. L.; Mao, F. F.; Zhang, X. H.; Yang, B. P.; Mao, J. G. $LiMg(IO_3)_3$: an Excellent SHG Material Designed by Single-site Aliovalent Substitution. *Chem. Sci.* **2019**, *10*, 10870−10875.
(61) Mao, F. F.; Hu, J. Y.; Li, B. X.; Wu, H. $Bi_4O(I_3O_{10})(IO_3)_3(SeO_4)$: Trimeric Condensation of IO_4^{3-} Monomers into the $I_3O_{10}^{5-}$ Polymeric Anion Observed in a Three-com-ponent Mixed-anion NLO Material. *Dalton Trans.* **2020**, *49*, 15597−15601.
(62) Mao, F. F.; Hu, C. L.; Chen, J.; Wu, B. L.; Mao, J. G. $HBa_{2.5}(IO_3)_6(I_2O_5)$ and $HBa(IO_3)(I_4O_{11})$: Explorations of Second-Order Nonlinear Optical Materials in the Alkali- Earth Polyiodate System. *Inorg. Chem.* **2019**, *58*, 3982−3989.
(63) Chen, J.; Chen, Q. Q.; Mao, F. F.; Liu, Z.; Li, B. X.; Wu, X. H.; Du, K. Z. $Ba_4Ag_5(IO_3)_6(I_3O_8)_3(I_4O_{11})_2$: A Nonlinear Optical Crystal Containing Two Types of Polyiodate Anions. *Inorg. Chem. Front.* **2022**, *9*, 5917−5925.
(64) Abudouwufu, T.; Zhang, M.; Cheng, S.; Zeng, H.; Yang, Z.; Pan, S. $K_2Na(IO_3)_2(I_3O_8)$ with Strong Second Harmonic Generation Response Activated by Two Types of Isolated Iodate Anions. *Chem. Mater.* **2020**, *32*, 3608−3614.
(65) Chen, J.; Hu, C. L.; Mao, F. F.; Yang, B. P.; Zhang, X. H.; Mao, J. G. REI_5O_{14} (RE = Y and Gd): Promising SHG Materials Featuring the Semicircle-Shaped $I_5O_{14}^{3-}$ Polyiodate Anion. *Angew. Chem., Int. Ed.* **2019**, *58*, 11666−11669.
(66) Phanon, D.; Gautier-Luneau, I. Promising Material for Infrared Nonlinear Optics: NaI_3O_8 Salt Containing an Octaoxotriiodate(V) Anion Formed from Condensation of $[IO_3]^-$ Ions. *Angew. Chem., Int. Ed.* **2007**, *46*, 8488−8491.
(67) Spaldin, N. A. A Beginner's Guide to the Modern Theory of Polarization. *J. Solid State Chem.* **2012**, *195*, 2−10.
(68) King-Smith, R. D.; Vanderbilt, D. Theory of Polarization of Crystalline Solids. *Phys. Rev. B* **1993**, *47*, 1651−1654.
(69) Godby, R. W.; Schluther, M.; Sham, L. Trends in Self-energy Operators and Their Corresponding Exchange-correlation Potentials. *J. Phys. Rev. B* **1987**, *36*, 6497−6500.

https://doi.org/10.1021/acs.inorgchem.2c04450
Inorg. Chem. XXXX, XXX, XXX−XXX